**Space Science Reviews manuscript No.**
(will be inserted by the editor)

# OpenGGCM Simulations for the THEMIS Mission

**Joachim Raeder[1 2], Douglas Larson[1], Wenhui Li[1], Emil L. Kepko[1], Timothy Fuller-Rowell[3]**

[1] Space Science Center, University of New Hampshire
[2] Physics Department, University of New Hampshire
[3] CIRES, Colorado University

Received: date / Revised version: date

**Abstract** The THEMIS mission provides unprecedented multi-point observations of the magnetosphere in conjunction with an equally unprecedented dense network of ground measurements. However, coverage of the magnetosphere is still sparse. In order to tie together the THEMIS observations and to understand the data better we will use the OpenGGCM global model of the magnetosphere - ionosphere system. OpenGGCM solves the magnetohydrodynamic (MHD) equations in the outer magnetosphere and couples via filed aligned current (FAC), electric potential, and electron precipitation to a ionosphere potential solver and the Coupled Thermosphere Ionosphere Model (CTIM). The OpenGGCM thus provides a global, comprehensive view of the magnetosphere - ionosphere system. An OpenGGCM simulation of one of the first substorms observed by THEMIS on March 23, 2007, shows that the OpenGGCM reproduces the observed substorm signatures very well, thus laying the groundwork for future use of the OpenGGCM to aid in the understanding of THEMIS data and ultimately to lead to a comprehensive model of the substorm process.

## 1 Introduction

The substorm "debate" has been a central part of space physics for over 4 decades and centers on the question as to what physical process(es) precipitate the sudden energy release in the magnetotail and the sudden auroral brightening and expansion [*Akasofu*, 1977; *Lui*, 1991; *Fairfield*, 1992; *Kennel*, 1992; *McPherron*, 1991; *Baker et al.*, 1999].

It is probably fair to say that it is widely accepted that substorms are ultimately powered by magnetic reconnection. Reconnection signatures are often observed in the tail during the course substorms. However, the location of the associated x-lines are typically observed ∼20 $R_E$ from Earth or further down the tail. On the other hand, the initial brightening of the aurora maps much closer to Earth. Thus, the question is commonly posed as to whether reconnection causes the process that brightens the aurora or whether the process that brightens the aurora causes reconnection. The THEMIS mission [*Sibeck and Angelopoulos*, 2008; *Angelopoulos*, 2008] is designed to answer this question by providing simultaneous measurements at 5 locations in order to establish how events proceed in time and space.

However, in spite of the unprecedented coverage ambiguities will likely remain because processes, such as dipolarization of the field or earthward flows may not necessarily occur strictly radially but sweep azimuthally over the spacecraft creating an apparent radial motion that does not correspond to the real one. Furthermore, substorms come in different sizes and shapes, and at this point it is only a hypothesis that they all follow the same scheme. It is well known that some substorms are triggered by various solar wind or IMF changes, while others occur spontaneous. Furthermore, there are other forms of geomagnetic activity, such as pseudo-breakups and Steady Magnetospheric Convection (SMC) events, that have some traits of substorms but differ in certain aspects. THEMIS will undoubtedly clarify the phenomenology and the relationships between different forms of activity and substorm triggers. However, the physical processes will not be understood fully until we are able to model them.

We will thus complement the THEMIS mission with global simulations of the magnetosphere. While it is possible to use local models to study isolated processes, such as reconnection, in detail, it is not possible to apply local models to substorms. Substorms are inherently global and encompass physical processes ranging from the dayside magnetopause, the lobes, the plasma sheet, and the inner magnetosphere to the ionosphere and to the ground. There have been a few attempts in the past to model substorms with global models, such as the "GEM substorm challenge" [*Slinker et al.*, 1995; *Fedder et al.*, 1995; *Wiltberger et al.*, 2000; *Raeder and Maynard*, 2001; *Raeder et al.*, 2001b]. None of these simulations have been able to reproduce a substorm in its entirety. Some substorm related phenomena are beyond the MHD description of the models, such as particle injections. However, even the phenomena that global MHD based models should be able reproduce do often not come out well. For example, all models have a tendency to enter a SMC-like state, where nightside reconnection closely balances dayside reconnection and no loading-unloading cycle occurs. Models then often require "tweaking" of parameters for a substorm to occur [*Raeder et al.*, 2001b]. However, global models keep improving with better numerics, better resolution, and better physical descriptions. Thus, one may expect that simulations will capture the physics of substorms with increasing realism in the near future. However, without checking the models against data one would not even know whether the physical processes in the model reflect reality or not. We will thus use the OpenGGCM in at least three different ways to support THEMIS and to better understand substorms:

1. We will test and constrain the model by simulating a number of substorm events with good THEMIS (and other) observations. These simulations will be driven with observed solar wind and IMF data which are usually available from solar wind monitors such as ACE or Wind. The output of these simulations will be critically compared –timetrace by timetrace– to the observations to find out what the model captures well and what not. Of course, the comparisons will never be perfect, and in many cases not good at all. We will run different simulations for one event with varying parameters, such as numerical resolution, M-I coupling parameters (see below), different anomalous resistivity, and different sub-models (ionosphere, ring current.) From these runs we will learn what parameters are important and how to choose them to get the physics right. We will also learn where we can trust the model, and which outputs will most likely differ from reality. In section 3 below we present an example, the March 23, 2007 substorm, which shows that the OpenGGCM gets several aspects of this substorm right, but not all.
2. Based on verification of the results as outlined above we will use the OpenGGCM results to help interpret the THEMIS data. For one, THEMIS observations are still spotty and leave large gaps in the spatial coverage, which can be filled with model results. Furthermore, the OpenGGCM can provide relationships that are generally not observable, such as the mapping between the plasma sheet and the ionosphere. This has also been done in the March 23, 2007 substorm example shown below. It turns out that the magnetic mapping using the OpenGGCM explains the observations much better than mapping based on empirical models [*Angelopoulos et al.*, 2008].
3. While the magnetosphere can not be controlled and manipulated like a laboratory experiment it can only be observed passively. Simulations, on the other hand, can be controlled within certain limits. For example, it is possible to use different solar wind and IMF, but it is not possible to reduce diffusion or resistivity below the inherent numerical diffusivities. We will thus use the OpenGGCM for numerical experiments to test hypotheses, for example, how solar wind and IMF changes trigger substorms, and how the ionosphere controls convection and the substorm process.

In the end, we hope that a new and more coherent picture of the substorm process will emerge from the THEMIS data in conjunction with OpenGGCM simulations. Without the simulations, the THEMIS data will likely leave ambiguities, while without the data the simulations would be in essence just speculation.

In the remaining sections we first describe the OpenGGCM in detail. Then we present first results of the March 23, 2007 substorm event, which is also discussed in a companion paper [*Angelopoulos et al.*, 2008]. That

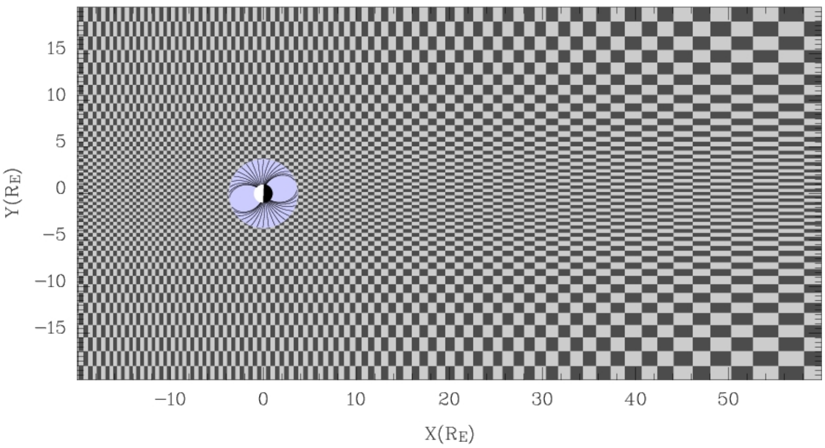


**Fig. 1** Please write your figure caption here

section also serves to illustrate some of the outputs that the OpenGGCM can produce. The last section summarizes our results and provides an outlook.

## 2 OpenGGCM Model

The OpenGGCM is a global coupled model of Earth's magnetosphere, ionosphere, and thermosphere. The magnetosphere part solves the MHD equations as an initial - boundary - value problem. The MHD equations are only solved to within $\sim 3\ R_E$ of Earth. The region within $3R_E$ is treated as a magnetosphere - ionosphere (MI) coupling region where physical processes that couple the magnetosphere to the ionosphere - thermosphere system are parameterized using simple models and relationships. The ionosphere - thermosphere system is modeled using the NOAA CTIM (Coupled Thermosphere Ionosphere Model [*Fuller-Rowell et al.*, 1996; *Raeder et al.*, 2001a]). In the following we describe each part of the model in more detail.

### *2.1 Outer Magnetosphere*

The physics of the outer magnetosphere is governed by the magnetohydrodynamic equations, which we use in their normalized, semi-conservative form:

$$\frac{\partial \rho}{\partial t} = -\nabla \cdot (\rho \mathbf{v}) \tag{1}$$

$$\frac{\partial \rho \mathbf{v}}{\partial t} = -\nabla \cdot (\rho \mathbf{v}\mathbf{v} + p\mathsf{I}) + \mathbf{j}\times\mathbf{B} \tag{2}$$

$$\frac{\partial e}{\partial t} = -\nabla \cdot (\{e + p\}\mathbf{v}) + \mathbf{j} \cdot \mathbf{E} \tag{3}$$

$$\frac{\partial \mathbf{B}}{\partial t} = -\nabla\times\mathbf{E} \tag{4}$$

$$\nabla \cdot \mathbf{B} = 0 \tag{5}$$

$$\mathbf{E} = -\mathbf{v}\times\mathbf{B} + \eta\mathbf{j} \tag{6}$$

$$\mathbf{j} = \nabla\times\mathbf{B} \tag{7}$$

$$e = \frac{\rho v^2}{2} + \frac{p}{\gamma - 1} \tag{8}$$

The symbols have their usual meaning, e.g., $\mathbf{B}$ and $\mathbf{E}$ are the magnetic and electric field, respectively, $\mathbf{v}$ is the plasma velocity, $\rho$ is the density, $p$ is the pressure, $\mathbf{j}$ is the current density, $\eta$ is a resistivity, $\mathsf{I}$ is the unit tensor, and $\gamma$ is the ratio of specific heats.

The semi-conservative formulation is chosen because it allows for difference schemes that numerically conserve of mass ($\varrho$), momentum ($\varrho\mathbf{v}$), and plasma energy ($e$), but with no strict conservation of total energy. Fully conservative schemes that conserve total energy ($U = \frac{p}{\gamma-1} + \frac{\rho v^2}{2} + \frac{B^2}{2}$) often suffer from instability in low $\beta$ regions where the pressure must be computed as the difference of two large quantites ($U$ and $B^2/2$), whereas the semi-conservative form avoids this difficulty.

The solution of the MHD equations in the outer magnetosphere is accomplished using an explicit second-order predictor-corrector finite difference time stepping scheme. The spatial derivatives are also computed using finite differences. However, because the simulation involves super-magnetosonic flows and shocks, simple finite differences are not sufficient but flux-limited schemes must be used. In case of the OpenGGCM we use a hybrid scheme that was originally proposed by Harten [*Harten and Zwas*, 1972], where we combine a fourth-order scheme with minimal diffusion error [*Zalesak*, 1979, 1981] with a the diffusive first-order Rusanov scheme. The numerical switch ensures that we obtain a high-order solution in regions of smooth variation of the flow, i.e., where there are no discontinuities, which degrades to a low order solution at discontinuities, such as shocks and contacts, where the high-order scheme would fail due to numerical dispersion. Such "shock-capturing" schemes are common in computational fluid dynamics of trans-sonic and super-sonic flows [*Hirsch*, 1990; *Laney*, 1998].

Maxwell's equation states that $\nabla\cdot\mathbf{B} = 0$ at all times, since there are no magnetic monopoles. Strictly speaking, this is only a initial condition for $\mathbf{B}$ because Faraday's law demands that if $\nabla\cdot\mathbf{B} = 0$ at some time it is to remain so as the magnetic field evolves, which can be seen from:

$$\nabla \cdot \frac{\partial \mathbf{B}}{\partial t} = \frac{\partial(\nabla\cdot\mathbf{B})}{\partial t} = -\nabla \cdot \nabla\times\mathbf{E} = 0 \tag{9}$$

Many numerical schemes do not *a priori* preserve $\nabla\cdot\mathbf{B}$. For such schemes the accumulation of $\nabla\cdot\mathbf{B}$ can lead to serious errors, in particular spurious parallel acceleration, wrong magnetic topology (field lines that are not closed), and significant errors in the shock jumps [*Brackbill and Barnes*, 1980; *Toth*, 2000]. There are a few methods to "clean" the magnetic field of monopoles, for example the projection method, but non of these are perfect and they also incur substantial additional cost [*Toth*, 2000]. The OpenGGCM uses the Constrained Transport (CT) method introduced by Evans and Hawley [*Evans and Hawley*, 1988] which employs a staggered grid that allows near perfect (to roundoff error) preservation of $\nabla\cdot\mathbf{B}$. With CT the magnetic field components are put on cell faces and the electric field components for the right hand side of Faraday's law are put on the centers of the cells' edges. Such staggered grids require interpolation for the coupling terms $\mathbf{j}\times\mathbf{B}$ and $\mathbf{j}\cdot\mathbf{E}$; however, this is a small price to pay for magnetic flux conservation.

An important aspect of every MHD code is the spatial grid. Many choices are possible, ranging from equidistant Cartesian grids to structured adaptive mesh refinement (AMR) grids [see *Raeder*, 2003, for an overview and discussion of grids]. The OpenGGCM employs a stretched Cartesian grid. Figure 1 shows a cut through the grid in the x-y plane at z=0. The figure shows only part of the grid, typically the grid extends to $\sim$20 $R_E$ in the sunward direction (to the left), several 100 $R_E$ in the anti-sunward direction (to the right), and $\sim$40 $R_E$ in the transverse (y,z) directions. Also, the grid resolution is substantially better than Figure 1 indicates, typically 0.1 - 0.2 $R_E$ at the sub-solar magnetopause and 0.2 - 0.3 $R_E$ in the near-Earth tail, with a total of $10^7$ - $10^8$ grid cells.

The primary advantage of the OpenGGCM grid is that it allows for a well load balanced and efficient parallelized code, while for the most part optimizing the resolution where it is needed. A uniform Cartesian grid would need $10^2$ - $10^3$ times the number of cells to achieve the same resolution in critical regions, such as the magnetopause or the plasma sheet. On the other hand, non-Cartesian or AMR grids may be able to optimize resolution better, but they also incur a higher computational cost and require much more complex codes.

### *2.2 Ionosphere and MI Coupling*

As outlined above, the MHD calculation only extends to $\sim$3 $R_E$ from Earth. At that inner boundary the MHD part of the model is coupled with the ionosphere, mainly by the closure of field-aligned currents (FACs) in the ionosphere. The OpenGGCM uses a static dipole model to map the FACs into the ionosphere, which is possible because the current density obeys a continuity equation and because these currents typically do not close across field lines at this altitude. At the ionosphere end a potential equation is solved on a sphere (or a section thereof) to yield the ionospheric convection potential [*Fedder and Lyon*, 1987]. The potential is then mapped back to the inner boundary of the MHD calculation where it is used as boundary condition for the flow and field integration ($\mathbf{v} = (-\nabla\Phi)\times\mathbf{B}/|B|^2$). Because the mapping originates at 3 $R_E$ it covers the latitudes from $\sim 58^0$ to $90^0$.

The ionosphere - thermosphere model CTIM is described in detail elsewhere [see *Fuller-Rowell et al.*, 1996, and references therein], thus we only provide a brief description here. CTIM is a global multi-fluid model of the thermosphere-ionosphere system with a long heritage. CTIM solves both neutral and ion fluid equations self-consistently from 80 to 500 km for the neutral atmosphere and from 80 to 10,000 km for the ionosphere on a spherical grid with 2° latitude resolution and 18° longitude resolution. The thermosphere part solves the continuity equation, horizontal momentum equation, energy equation, and composition equations for the major species O, $O_2$, and $N_2$ on 15 pressure levels. The ionosphere model part solves the continuity equations, ion temperature equation, vertical diffusion equations, and horizontal transport for $H^+$ and $O^+$, while chemical equilibrium is assumed for $N_2^+$, $O_2^+$, $NO^+$, and $N^+$. The horizontal ion motion is governed by the magnetospheric electric field. The coupled model includes about 30 different chemical and photo-chemical reactions between the species. Compared to the magnetosphere, the CTIM time scales are relatively long, allowing for numerical time steps of the order of 1 minute. Consequently, CTIM is computationally very efficient and runs considerably faster than real-time (>10 times) on a single CPU.

CTIM's primary input are the solar UV and EUV flux (parameterized by the solar 10.7 cm radio flux), the tidal modes (forcing from below), auroral electron precipitation parameters, and the magnetospheric electric field.

The electron precipitation parameters, energy flux $F_E$ and mean energy $E_0$ are computed separately for diffuse precipitation and for discrete precipitation, i.e., for electrons accelerated in regions of upward FAC.

Diffuse precipitation is parameterized by:

$$F_E = n_e (kT_e/2\pi m_e)^{\frac{1}{2}} \qquad , \qquad E_0 = kT_e \tag{10}$$

where $T_e$ and $n_e$ are the magnetospheric electron temperature and density, respectively, and $k$ is the Boltzmann constant.

Discrete electron precipitation is modeled using the Knight relation [*Knight*, 1972]:

$$\varDelta\Phi = K \max(0, -j_{\|}) \tag{11}$$

$$K = \frac{e^2 n_e}{\sqrt{2\pi m_e k T_e}} \tag{12}$$

$$F_E = \varDelta\Phi_{\|} j_{\|} \qquad , \qquad E_0 = e\varDelta\Phi_{\|} \tag{13}$$

where $\Delta\Phi$ is the parallel potential drop on an auroral field line. Because the MHD model cannot provide an electron temperature we use the MHD single fluid temperature adjusted by a fudge factor.

The electric field in the ionosphere is assumed to be a potential field and is obtained from current conservation, which leads to the following potential equation [*Vasyliunas*, 1970; *Kelley*, 1989]:

$$\nabla \cdot \mathbf{\Sigma} \cdot \nabla\Phi = -j_{\parallel} \sin I \tag{14}$$

with the boundary condition $\Phi$=0 at the magnetic equator. Because the ionosphere is a magnetized and partially ionized plasma the ionospheric conductance is a tensor [*Strangeway and Raeder*, 2001], given by:

$$\mathbf{\Sigma} = \begin{pmatrix} \Sigma_{\theta\theta} & \Sigma_{\theta\lambda} \\ -\Sigma_{\theta\lambda} & \Sigma_{\lambda\lambda} \end{pmatrix} \tag{15}$$

$$\Sigma_{\theta\theta} = \frac{\Sigma_P}{\sin^2 I} \quad , \quad \Sigma_{\theta\lambda} = \frac{\Sigma_H}{\sin I} \quad , \quad \Sigma_{\lambda\lambda} = \Sigma_P \tag{16}$$

where $\Sigma_H$ is the Hall conductance, $\Sigma_P$ is the Pedersen conductance, $\theta$ is the magnetic latitude, $\lambda$ is the magnetic longitude, and $I$ is the magnetic field inclination.

The ionospheric Hall and Pedersen conductance is computed by CTIM from first principles, i.e., from the electron - neutral collision terms. In addition the neutral wind dynamo is explicitly included in the solution of the electric potential.

Figure 2 shows a block diagram of the OpenGGCM elements and how they relate to each other. The connection arrows indicate the flow of data. At present time not all of the elements are implemented yet. The field line integration, ring current, and radiation belt module are still works in progress. However, these pieces are not crucial for substorm studies.

Note that the OpenGGCM only requires a minimal set of inputs. The solar wind and IMF are typically taken from a solar wind monitor, such as ACE or Wind. Geotail and Cluster can also provide SW and IMF data when they are upstream of the bow shock. Such data taken closer to Earth are preferable because they better represent the solar plasma and fields that ultimately interact with the magnetosphere. However, even these data are not perfect as input for the OpenGGCM because they generally lack information about the three dimensional solar wind structure which needs ideally to be known to specify the time dependent MHD variables across the entire inflow boundary. We thus need to make an assumption as to the structure of the solar wind. One option is to assume that the solar wind parameters are independent of $Y_{GSE}$ and $Z_{GSE}$. In that case the IMF $B_x$ component cannot change in time because that would violate $\nabla \cdot \mathbf{B} = 0$. If there are significant IMF $B_x$ variations the assumption of $Y_{GSE}$ and $Z_{GSE}$ independence cannot be true. In that case we attempt to find a direction $\mathbf{N}$ in the solar wind such that the magnetic field component along that direction ($B_N$) does not change significantly. Since usually only one solar wind monitor is available

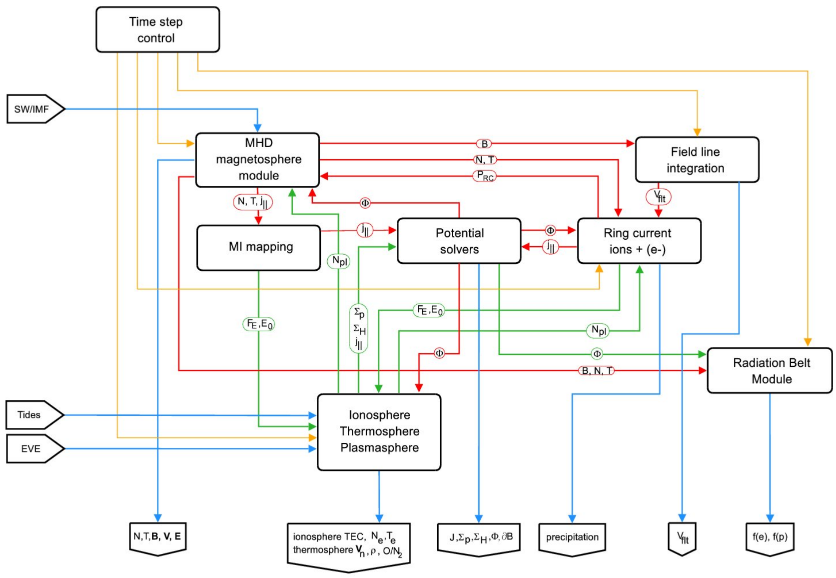


**Fig. 2** Block diagram of the CGM with its models and with data/control flow. Blue lines denote model input and output. Red lines denote data flow with strong coupling. Green lines denote data flow with weak or slow coupling. Orange lines denote control flow. B, N, and T are the magnetospheric magnetic field, plasma density, and temperature, respectively. $j_{\|}$ is the field aligned current, $\Phi$ the ionosphere potential, $N_{PL}$ the plasmasphere density, $F_E$ and $E_0$ the energy flux and mean energy of precipitating electrons, $\Sigma_H$ and $\Sigma_P$ the ionosphere Hall and Pederesen conductances, $\partial B$ is the ground magnetic perturbation, $P_{RC}$ the ring current pressure, and $V_{flt}$ the magnetic flux tube volume.

we employ the minimum variance method of *Sonnerup and Cahill* [1967, 1968] to find that direction. We call this the MINVAR method. If observations from multiple solar wind monitors are available more precise methods are available [see, for example *Russell et al.*, 2001]. If $B_N$ is fairly constant over the time interval of interest we set $B_N$ to be constant in time at the value of its average and then transform the field back into GSE coordinates and use it as input to the MHD model. In this case the solar wind and IMF convects into the model as sheets whose orientation is given by their normal vector **N**.

In the case that $B_N$ from the minimum variance transform is not nearly uniform (defined such that the variance of $B_N$ is significantly smaller, say <10 %, of the total field) one is in the unfortunate situation that the solar wind does not have a simple sheet-like structure. There is also not enough information available to determine the structure, so one is left with the option to either ignore the IMF $B_x$ component or set it to some constant value

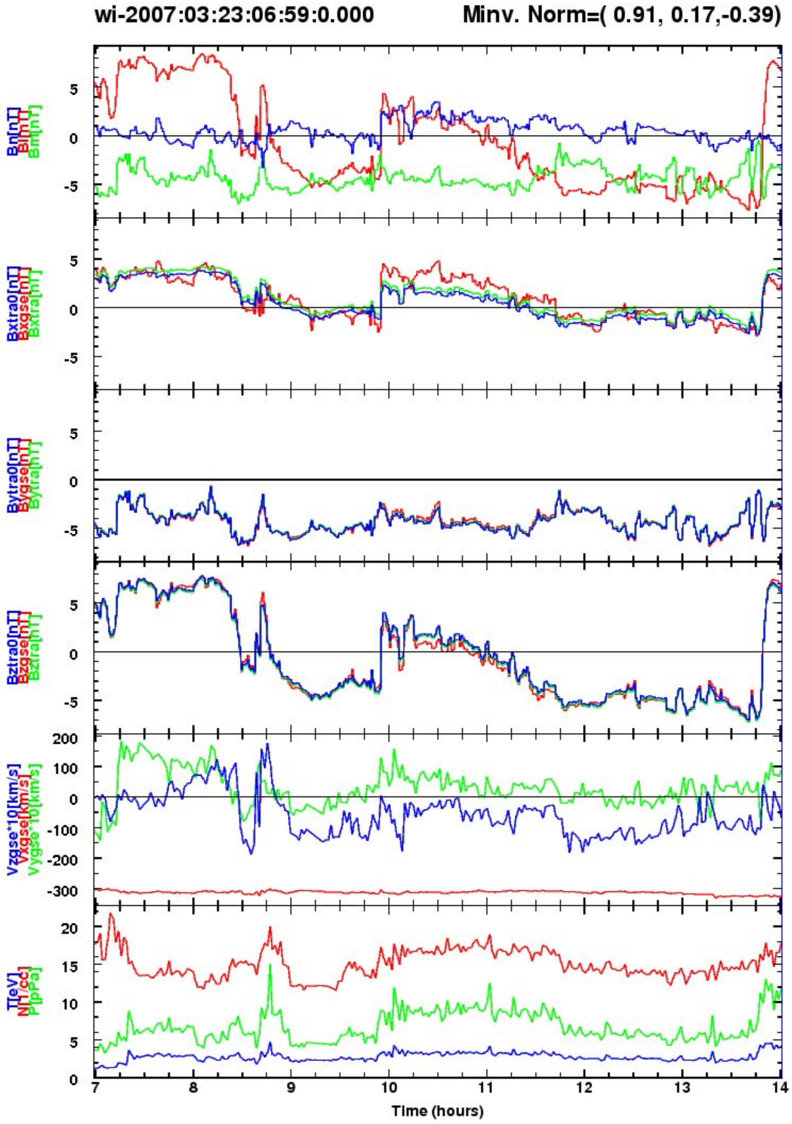


**Fig. 3** Solar wind and IMF data processed by the MINVAR procedure and used as input for the simulation of the March 23, 2007 substorm event.

that seems reasonable. This may in many cases not be a bad choice, because the IMF $B_x$ component essentially does not contribute to the interplanetary electric field (IEF) and because the draping of the IMF around the magnetosphere normally reduces the $B_x$ component before the field interacts with the magnetosphere. However, if the IMF $B_x$ component dominates the IMF it may affect the reconnection geometry at the magnetopause and one needs to carefully assess the simulation results for their validity.

Figure 3 shows time series of the solar wind and IMF data observed by Wind for the March 23, 2007 substorm, along with the data that have been processed using the MINVAR procedure. The top panel shows the $B_L$ (maximum variance, red line), $B_M$ (intermediate variance, green line), and $B_N$ (minimum variance, blue line) IMF components. The eigenvector (direction) corresponding to the minimum variance $\mathbf{N}$ is given at the top of the figure. The direction of $\mathbf{N}$ is close to sunward but has a significant $Z$ component. For this case the variance of the $B_N$ component is small compared to the total field, thus the IMF must at least locally be ordered in sheets that are normal to $\mathbf{N}$. There are several discontinuities, i.e., rapid changes in the IMF direction, in this interval. Since $B_N$ across these discontinuities is close to zero they are most likely tangential discontinuities.

The following three panels show the three IMF components. The red lines show the Wind observations. The blue lines show the result from setting $B_N$ to zero and transforming back to GSE. The green lines show the result from setting $B_N$ to its average over the entire interval and transforming back to GSE. For each component the three lines nearly coincide. The near coincidence of the green and blue lines simply reflects the fact that the $B_N$ average is nearly zero for this interval. The near coincidence of the red and green traces shows that the IMF model of inclined planar sheets whose normal is $\mathbf{N}$ is consistent with the data.

The bottom 2 panels of Figure 3 show the solar wind plasma parameters. These time series are not affected by the MINVAR procedure. However, in order to be consistent with the treatment of the plasma parameters are convected into the simulation box in the same manner as the field components, i.e., the MHD state vector $\mathbf{U} = (\mathbf{B}, \mathbf{V}, N, T)$ at the inflow boundary is not just a function of time $\mathbf{U}(t)$, but also a function of $Y_{GSE}$ and $Z_{GSE}$ ($\mathbf{U}(y, z, t)$) to take into account the inclined sheet structure of the solar wind and IMF.

## 3 OpenGGCM Products and the March 23, 2007 Substorm Example

The OpenGGCM produces the three-dimensional grids with the MHD state vector ($\rho$,$p$,$\mathbf{V}$,$\mathbf{B}$), along with a number of ionosphere and thermosphere quantities, such as the ionosphere potential, ionospheric currents, electron density, neutral composition, and neutral winds. These quantities describe the state of the system, however, they often cannot be directly compared to observations, and the information contained in the gridded fields is too overwhelming to "see" the physical processes that occur and to draw conclusions. The output of a simulation run can easily exceed one TB (terabyte, equal to $10^{12}$ bytes) of data. Thus, in order to extract useful information a substantial amount of post-processing and visualization is necessary. There are many ways to extract information from the raw data and new techniques are still being developed. In the following we demonstrate some of the most basic techniques and applications. We will use an OpenGGCM simulation of the March 23, 2007 substorm as an example. This substorm is also discussed elsewhere in this issue [*Angelopoulos et al.*, 2008; *Keiling et al.*, 2008], thus we will not discuss the observations here but direct the reader to these papers.

### *3.1 Satellite time series*

The most basic comparison is that of the moments and fields measured at the satellite with time series taken in the simulation at the same location. We refer to these time series as "virtual satellites". In version 3.1 of the OpenGGCM these time series are automatically generated for a number of satellites (made up or real) and their trajectories, which are input to the model. This has the advantage that time series output can be generated at high cadence (~5 s) but it does not allow to re-position the virtual satellite after the run is completed. The latter is sometimes useful when a satellite is located close to a boundary. In that case a small error in the boundary location can lead to a complete mismatch between the observations and the virtual satellite. By placing a second virtual satellite at the other side of the boundary, often just by a fraction of 1 $R_E$ one can then show that the boundary location is primarily in error, not the MHD state variables themselves.

Figures 4-6 show the comparison of the virtual satellites THEMIS C, THEMIS B, and THEMIS E with the in situ observations. THEMIS C is closest to the tail center, THEMIS E is closest to the dusk flank, and THEMIS D, B, and A are located very close together between C and E, and thus observe nearly the same, at least on the MHD time scale. The companion paper [*Angelopoulos et al.*, 2008] discusses the locations in detail.

All 3 satellites observe a flow burst, both tailward and duskward, near the time of the substorm onsets, which was determined by Angelopoulos et al. [2008] to occur at 10:54 UT (minor activation) and 11:18:45 UT (major activation). At the same time the magnetic field becomes strongly deflected. That deflection is similar, but not the same, as a classical dipolarization. The $B_z$ and $B_y$ components increase like in a dipolarization, however, the magnitude of $B_x$ also increases, which is opposite to dipolarization. Furthermore, the sunward flows sweep colder and denser plasma past the spacecraft.

The virtual spacecraft "see" essentially the same signatures, but with some significant differences. First, the substorm onset, as defined by the

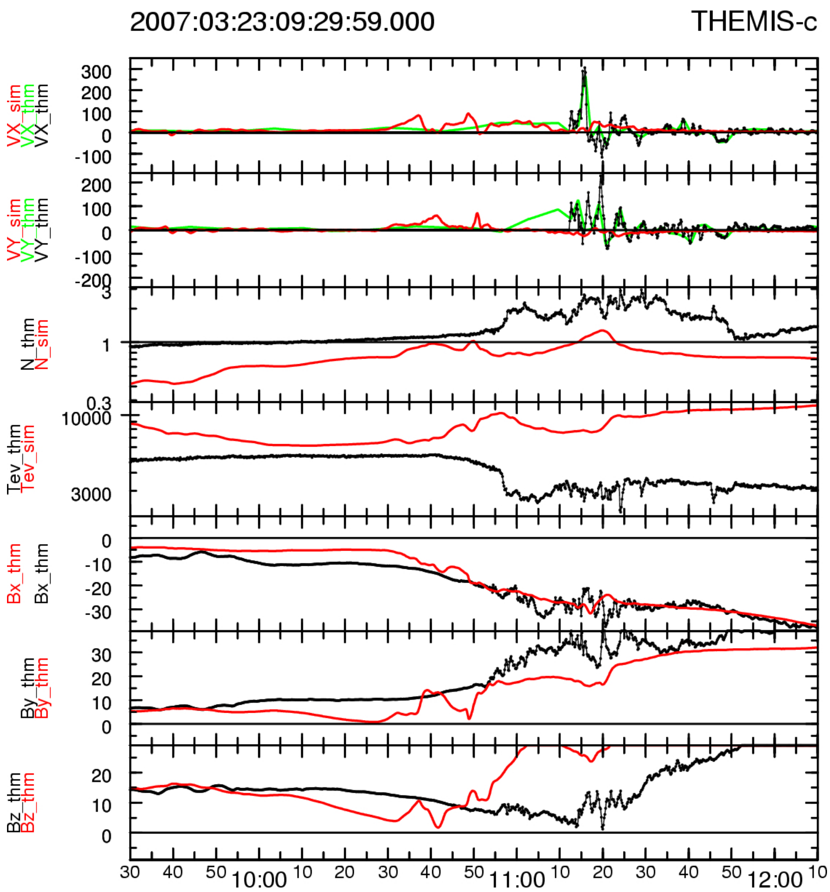


**Fig. 4** Comparison of the MHD state variables measured by THEMIS C (black and green lines, the latter are from on-board computation of moments) and from the OpenGGCM simulation (red lines). The panels show, from top to bottom: the 3 components of the velocity, the plasma number density, the ion temperature, and the 3 components of the magnetic field. All variables are in GSE coordinates. THEMIS C is closest to the tail center.

onset of fast flows here, occurs too early, ~1040 UT, as opposed to the 10:54 UT and 11:19 UT onsets and intensifications observed by THEMIS and the imagers [see Angelopoulos et al., 2008, this issue]. This is also borne out in the aurora from the simulation discussed further below. However, the general pattern of the magnetic field and flow variations are quite well reproduced. Plasma density an temperature match least well, which can be understood as a memory effect of the magnetosphere. This simulation was started at 07:00 UT, i.e., 4 hours before the substorm onset, thus much of the plasma in the simulated magnetosphere may still be primordial, i.e., remnant from the initial conditions. How long it takes for the magnetosphere

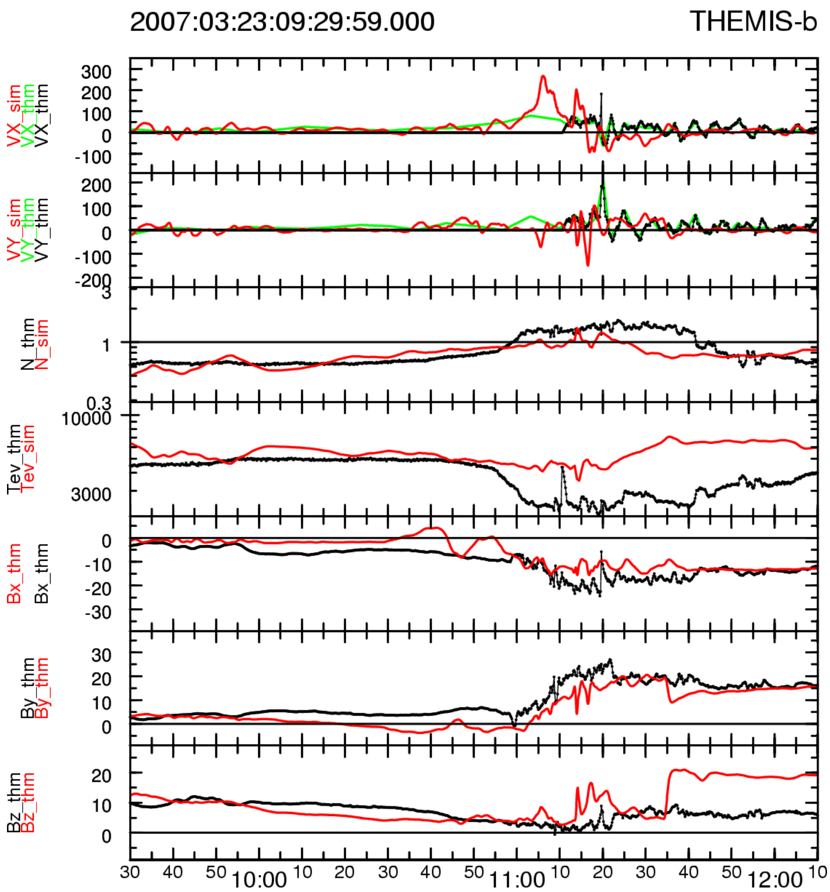


**Fig. 5** Comparison of the MHD state variables measured by THEMIS B in the same format as Figure 4. THEMIS B is the middle spacecraft between C and E.

to completely replenish all of its plasma from the solar wind and ionospheric sources is not well know and probably depends on the solar wind and IMF conditions.

Overall one can say that the simulation reproduces the key observational features well enough for one to have confidence in the results. In particular, a decent comparison like this one can be the starting point for a more detailed analysis of the simulation in order to elucidate the processes that lead to the observed phenomena.

### *3.2 Ionosphere and aurora*

Of course, the defining characteristic of a substorm is the brightening of the aurora and the development of the westward traveling surge (WTS) [*Akasofu*, 1977, 1964]. The OpenGGCM does not produce auroral emissions,

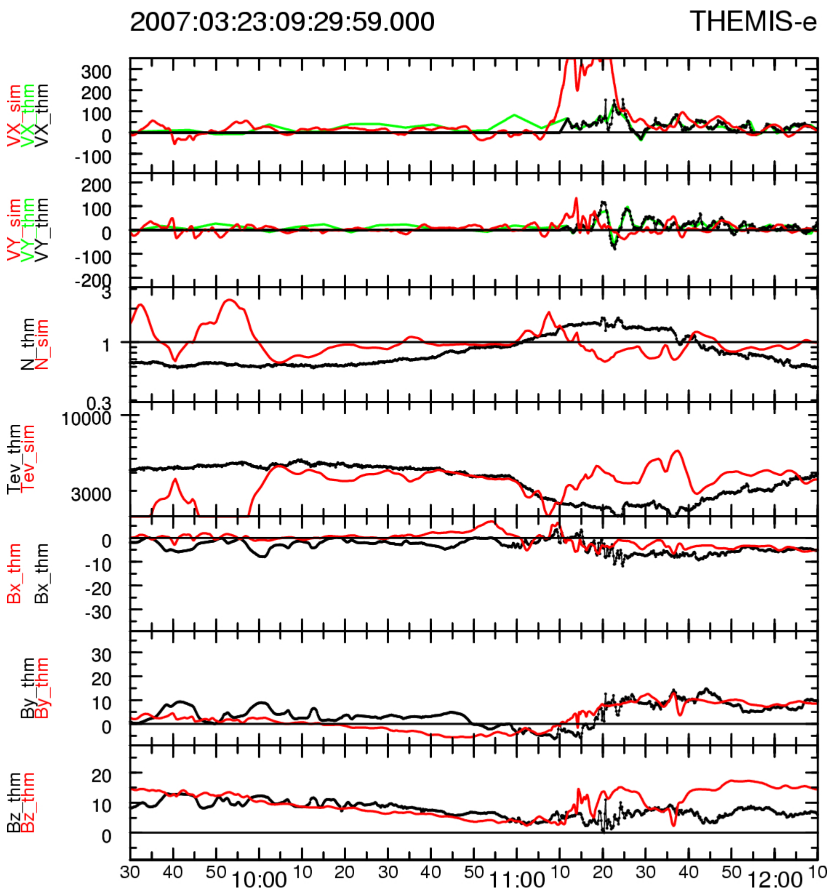


**Fig. 6** Comparison of the MHD state variables measured by THEMIS E in the same format as Figure 4. THEMIS E is the spacecraft closest to the dusk flank.

however, it does produce the energy flux and the mean energy of two populations of precipitating electrons. The first population is the thermal electron flux from the inner magnetosphere, which is unstructured and representative of the diffuse aurora. The second population is made up of electrons that have been accelerated in regions of upward flowing field-aligned current (FAC), as discussed in section 2. This population is highly structured and it is considered generating the discrete aurora, although that distinction may not be made from an experimental view. In high resolution OpenGGCM runs, such as the one presented here, features in the discrete precipitation as small as $\sim 0.5^\circ$ in latitude and $\sim 2^\circ$ in longitude can be resolved. In the plots discussed below we show the energy flux of these accelerated electrons as a proxy for auroral emissions. In principal the emissions could be calculated [*Emery et al.*, 1996; *Germany et al.*, 1997; *Lummerzheim et al.*, 1997]. However, in order to be able to compare the emissions to data one also

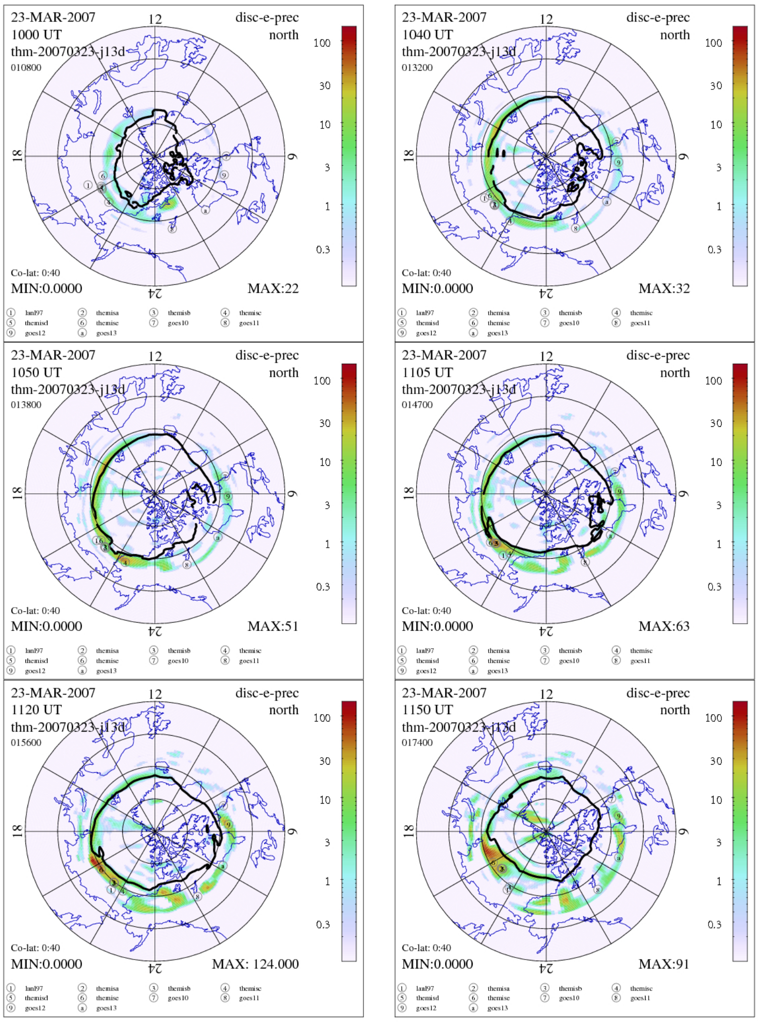


**Fig. 7** Polar view of the northern hemisphere. The color coding shows the energy flux of accelerated electrons, which serves as a proxy for auroral emissions. The thick black line is the polar cap boundary.

needs to model the specific instrument responses, which has not been done here.

Figure 7 shows a polar view of the northern hemisphere at 6 different times. Each of the 6 panels shows color coded the energy flux of precipitating electrons in units of mW/m. The thick black line shows the polar cap boundary, i.e., the boundary between open and closed magnetic flux. Each panel has the date and the UT time indicated in the upper left corner.

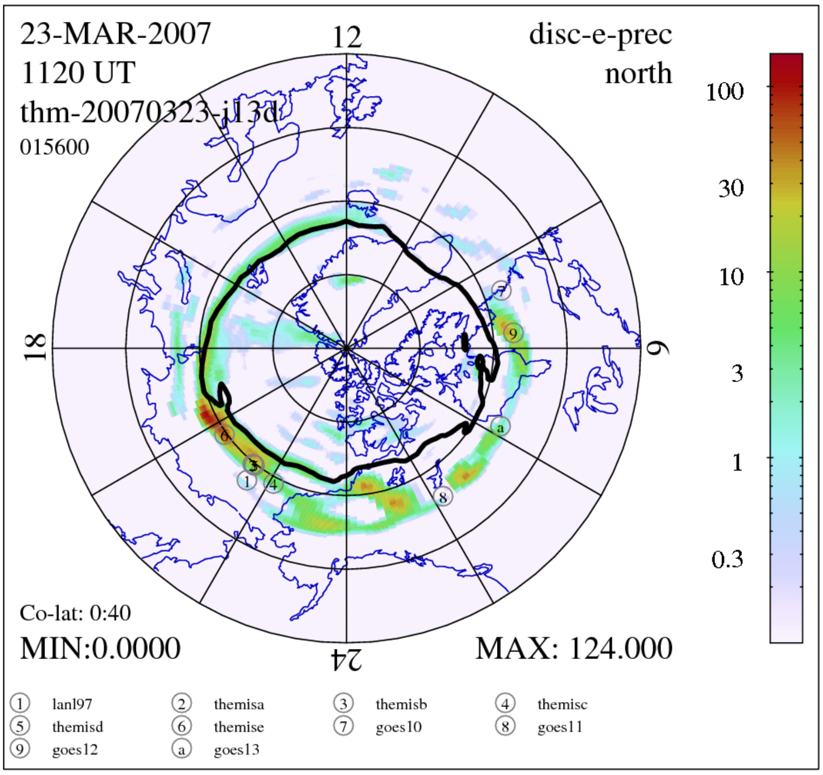


**Fig. 8** Panel 5 of Figure 7 at a larger size. The magnetic footpoints of several satellites show that the THEMIS probes map right into the westward traveling surge.

At 10:00 UT the IMF at the magnetopause is still northward and thus the magnetosphere is in a geomagnetically quiet state. The polar cap (PC) is small, with the PC boundary (PCB) mostly located between 75° and 80° magnetic latitude. At 10:40 UT the IMF has turned southward at the dayside magnetopause. The PC has expanded considerably, with the PCB located just above 70° at most local times. This state represents the growth phase of the substorm, i.e., magnetic energy is being convected into and stored in the tail lobes. As the tail lobes expand, so does the PC, and at the same time the magnetic flux and magnetic energy in the lobes ($B^2/2\mu_0$) increases. During the quiet time and during the growth phase the discrete aurora occurs primarily just equatorward of the PCB.

At 10:50 UT the first indication of a substorm onset becomes visible near 22.5 MLT and 68° magnetic latitude. Closer inspection of the time series of polar plots shows that this intensification already started at 10:44 UT. This is considerably earlier than the first onset in the data, where the first intensification occurred at ∼10:54 UT, followed by intensifications at ∼11:10 UT and ∼11:19 UT [*Angelopoulos et al.*, 2008]. The next panel shows that by 11:05 UT the aurora had expanded northward by ∼3° and westward to ∼21 MLT. Close inspection of the following 10 min (not shown here) shows that the expansion slows down and stops. However, between 11:15 UT and 11:20 UT another intensification starts that causes a significant further expansion westward to ∼19 MLT and ∼77° magnetic latitude, as can be seen in the 5th and 6th panel. This latter expansion appears to correspond to the 11:19 UT expansion observed in the data. Comparison with the IMF data shown in Figure 3 indicates that this intensification is likely caused by the sharp northward turn of the IMF at 09:55 UT. The Wind data need to be time shifted by ∼75 min to account for the convection time from the Wind location ($X_{GSE} = 198\ R_E$) to the magnetopause, which puts the arrival of the northward turning at the magnetopause at ∼11:10 UT. There is considerable uncertainty in the actual arrival time because Wind is off the sun-Earth line by ∼30 $R_E$.

In Figure 7 we also marked the magnetic mapping from the THEMIS (and several other) satellites to the ionosphere. For clarity we repeat the 5th panel of Figure 7, shown as Figure 8. The THEMIS probes map magnetically into the path of the WTS. One would have expected this because of the flow and field signatures observed by THEMIS and on the ground. However, magnetic mapping using an empirical magnetic field model places the THEMIS probes east and south of the WTS [*Angelopoulos et al.*, 2008], thus the OpenGGCM mapping is much more realistic.

### *3.3 Magnetosphere flow and field evolution*

In order to understand the physical processes that trigger the expansion phase onset and that provide the power in the expansion phase one needs to analyze the complete three-dimensional data sets from the simulation. This is a difficult task because one has to deal with huge data sets in 4 dimensions, i.e., 3 space dimensions and time. The simulation of the substorm shown here has $\sim 30\times 10^6$ cells, and one needs to compose at least a few hundred snapshots in time to obtain a complete picture. Furthermore, there are at least the 8 MHD state variables per cell, and in practice one needs to examine a number of derived variables, such as current density or electric field. In all, the simulation leads to $10^{11}$ to $10^{13}$ data values, which are impossible to comprehend all together. Furthermore, our data presentation techniques and tools are mostly restricted to a two-dimensional “flatland” (paper, computer screen) which requires a substantial reduction and projection of the data [*Tufte*, 1990]. Occasionally one can add the time dimension with movies, but even in those one can only see some 3-dimensional hyperspaces out of the 4-dimensional data that matter.

Figure 9 shows 3 three-dimensional renderings of the magnetosphere in the vicinity of the THEMIS probes. Each rendering is composed of 3 cut planes (at $X_{GSE}$=0$R_E$ , $Y_{GSE}$=0$R_E$ , $Z_{GSE}$=-2$R_E$ ), which are color coded

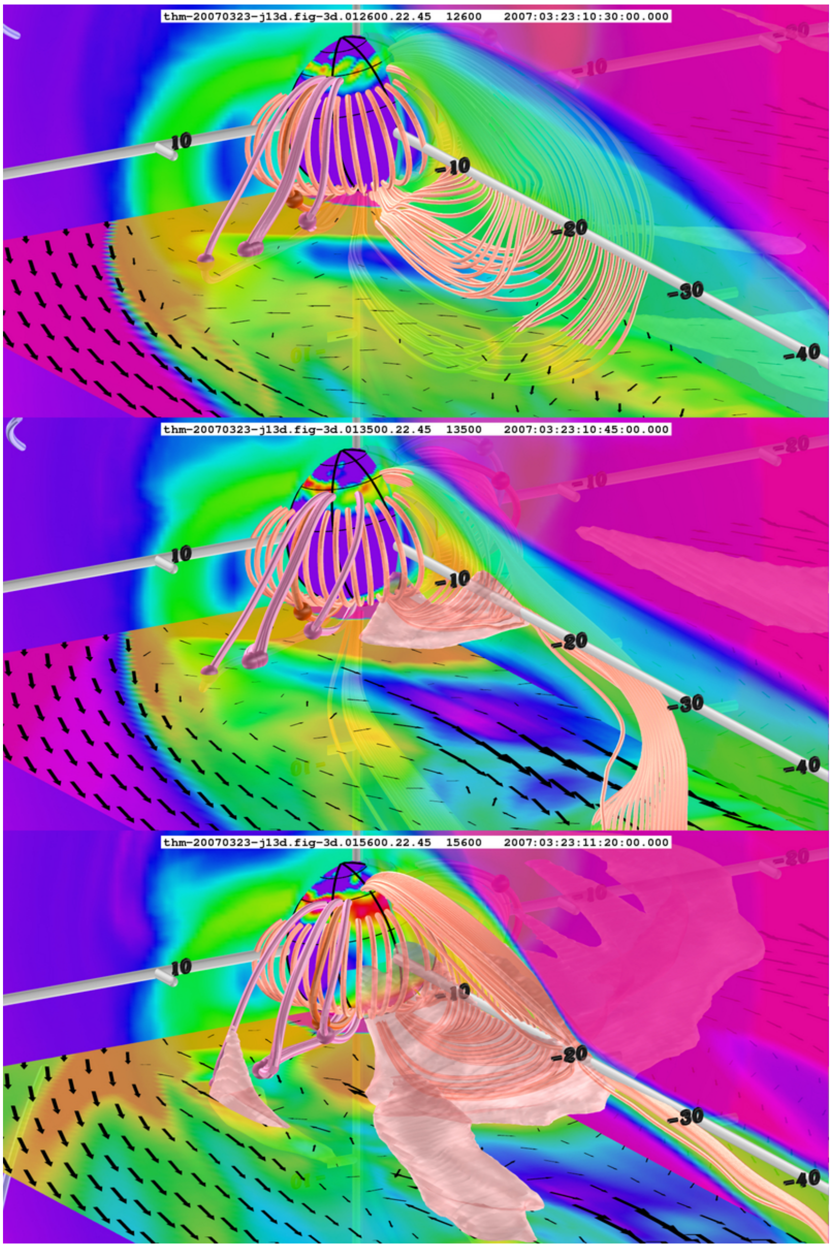


**Fig. 9** Three-dimensional rendering of the magnetosphere configuration in the vicinity of the THEMIS probes during the March 23, 2007 substorm event. See text for a detailed explanation.

according to a physical quantity, such as $B_z$ in the $Z_{GSE}$=-$2R_E$ plane and log($T$) in the other 2 planes. The $Z_{GSE}$=-$2R_E$ also shows arrows that depict the flow velocity. These arrows are scaled to $\sqrt{V}$ in order to cover a large dynamic range of speeds. The sphere about the origin has a radius of $3.5R_E$ and coincides with the inner boundary of the MHD simulation. Its surface is also color coded, in this case with the Hall conductance, which has been mapped along dipole field lines from the ionosphere. A number of field lines is drawn as pink tubes. One set of field lines originates from 65° magnetic latitude, every 7.5° longitude. These field lines are all dipolar and mostly undisturbed. They provide a good idea of the dipole orientation. A second set of field lines is seeded along the X-axis in the tail. These field lines are obviously highly dynamic. Satellites of interest are pictured by spheres, and field lines are drawn through them. In Figure 9, these satellites are, in order of decreasing distance, THEMIS E, A, B, D, C, and LANL97, which is a geosynchronous satellite and closest to Earth. Finally, there is a pink iso-surface that depicts sunward flows in excess of 180 km/s.

The top panel of Figure 9 shows the magnetosphere at 10:30 UT, which is during the substorm growth phase. At this time the $B_z$ in the plasma sheet is positive, i.e., the plasma sheet is on closed field lines. However, the field is not simply dipolar, but significantly stretched. Also, the negative IMF $B_y$ exerts a twist on the tail which is clearly visible. The flows in the plasma sheet are mostly calm and of the order of a few 10s km/s.

The second panel shows the tail during the first substorm activation, at 10:45 UT. There is now a significant patch of negative $B_z$ in the plasma sheet at $X_{GSE}\sim$-$20R_E$ and somewhat duskward of the tail center. This negative $B_z$ is also accompanied by strong tail ward flows of several 100 km/s. Note that a negative $B_z$ closer to Earth can also arise from the dipole tilt and the fact that the $Z_{GSE}$=-$2R_E$ plane does not coincide everywhere with the center of the plasma sheet. Such negative $B_z$ comes from southern lobe field lines that bend towards the Earth into the southern polar cap. Coincident with the tailward flows are also earthward flows closer to Earth. These are not visible in the $Z_{GSE}$=-$2R_E$ plane, but in the iso-surface that extends earthward of the reconnection site. At this time not much has happened at the THEMIS and LANL locations, but there are clear enhancements in the ionosphere Hall conductance visible. These occur because a substorm current wedge has formed that causes enhanced electron precipitation in the ionosphere at ∼22 MLT.

The bottom panel shows the tail at 11:20 UT, just after the second intensification. At this time, the field near midnight has already dipolarized. There is now a new reconnection event further duskward. This event also creates a patch of strong southward IMF and both earthward/sunward and tailward flows. Most importantly, the sunward flows engulf the THEMIS spacecraft and cause the field at the spacecraft to dipolarize. Comparison with Figures 4-6 shows that these flows and the dipolarization of the field are indeed observed.

Although Figure 9 reveals a lot about the structure of the tail and its time evolution it only shows some very limited aspects of the physical processes occurring in the simulation. The explanatory power of such Figures depends significantly on what one chooses to show and how it is shown. If one replaces the sequence of the snapshots in time with a movie one can get a much better impression of the dynamics of the plasma sheet. However, even then, the careful selection of the visualizing elements, such as cut planes or field lines is crucial to exhibit the dynamical evolution. This will still require a substantial amount of work in the future.

## 4 Summary and Conclusions

In this paper we presented a description of the OpenGGCM and its role in supporting the THEMIS mission. For the simulations to be useful we first need to show that the model indeed produces the observed dynamical changes in the magnetosphere and ionosphere. The comparison of the model results with observations will never be perfect. However, as long as the model produces the essential features, one can have confidence in the model results and one can draw conclusions from the model results. We have presented here the first of such comparisons and shown that the model reproduces most of the salient features of the March 23, 2007, substorm. We have shown how the model can contribute to the mission and data analysis; in this case by providing the magnetic mapping between the ionosphere and the plasma sheet. We also provided a first glimpse at how the model results can be used to investigate the physical processes that ultimately lead to the observations.

In the future many more comparisons between the model and data need to be done to firmly establish what the model gets right and what not. With that background the OpenGGCM can then be used to analyze the underlying physics in detail. Furthermore the model can be used to conduct numerical experiments and to ask specific questions. For example, we may use the model to establish what mechanism leads to substorm triggering by northward turnings of the IMF. Comparing a run with a substorm triggered by a NBZ turn to one that is otherwise identical but without NBZ turn should provide the clues. Similarly, one can investigate the role that various parameters play in the onset mechanism, such as anomalous resistivity, or ionosphere conductance. Such studies should eventually lead to a clearer, and less controversial, picture of the substorm process.

*Acknowledgements* This research was supported by NASA grant NAS5-02099. Development of the OpenGGCM has been supported by NASA grant NNG05GM57G and NSF grants ATM-0639658. Part of the simulations were performed at the San Diego Supercomputer Center and at the National Center for Supercomputer Applications.

## References


Akasofu, S.-I., The development of the auroral substorm, *Planet. Space Sci.*, *12*, 273, 1964.

Akasofu, S.-I., *Physics of Magnetospheric Substorms*, Reidel, Dordrecht, 1977.

Angelopoulos, V., The THEMIS mission, *Space Sci. Rev.*, *this issue*, submitted, 2008.

Angelopoulos, V., et al., First results from the THEMIS mission, *Space Sci. Rev.*, *submitted*, 2008.

Baker, D. N., T. I. Pulkkinen, J. Büchner, and A. J. Klimas, Substorms: A global instability of the magnetosphere-ionosphere system, *J. Geophys. Res.*, *104*, 14,601, 1999.

Brackbill, J. U., and D. C. Barnes, The effect of nonzero div B on the numerical solution of the magnetohydrodynamic equations, *J. Comp. Phys.*, *35*, 426, 1980.

Emery, B. A., et al., Comparing POLAR UVI imager data and other conductance sources in AMIE, *Eos Trans. AGU*, *77(46)*, 613, 1996.

Evans, C. R., and J. F. Hawley, Simulation of magnetohydrodynamic flows: A constrained transport method, *Astrophys. J.*, *332*, 659, 1988.

Fairfield, D. H., Advances in magnetospheric storm and substorm research: 1989–1991, *J. Geophys. Res.*, *97*, 10,865, 1992.

Fedder, J. A., and J. G. Lyon, The solar wind - magnetosphere - ionosphere current - voltage relationship, *Geophys. Res. Lett.*, *14*, 880, 1987.

Fedder, J. A., S. P. Slinker, J. G. Lyon, and R. D. Elphinstone, Global numerical simulation of the growth phase and the expansion onset for a substorm observed by Viking, *J. Geophys. Res.*, *100*, 19,083, 1995.

Fuller-Rowell, T. J., D. Rees, S. Quegan, R. J. Moffett, M. V. Codrescu, and G. H. Millward, A coupled thermosphere-ionosphere model (CTIM), in *STEP Report*, edited by R. W. Schunk, p. 217, Scientific Committee on Solar Terrestrial Physics (SCOSTEP), NOAA/NGDC, Boulder, Colorado, 1996.

Germany, G. A., G. K. Parks, M. Brittnacher, J. Cumnock, D. Lummerzheim, J. F. Spann, L. Chen, P. G. Richards, and F. J. Rich, Remote determination of auroral energy characteristics during substorm activity, *Geophys. Res. Lett.*, *24*, 995, 1997.

Harten, A., and G. Zwas, Self-adjusting hybrid schemes for shock computations, *J. Comput. Phys.*, *9*, 568, 1972.

Hirsch, C., *Numerical Computation of Internal and External Flow*, vol. II, John Wiley, New York, 1990.

Keiling, A., et al., Correlation of substorm injections, auroral modulations, and ground Pi2, *Geophys. Res. Lett.*, *submitted*, 2008.

Kelley, M. C., *The Earth's Ionosphere*, Academic Press, New York, 1989.

Kennel, C. F., The Kiruna conjecture: The strong version, in *Substorms I*, vol. ESA SP-335, p. 599, Paris, 1992.

Knight, S., Parallel electric fields, *Planet. Space Sci.*, *21*, 741, 1972.

Laney, C. B., *Computational Gasdynamics*, Cambridge University Press, 1998.

Lui, A. T. Y., Extended consideration of a synthesis model for magnetic substorms, in *Magnetospheric Substorms*, edited by J. R. Kan, T. A. Potemra, S. Kokubun, and T. Ijima, vol. 64, p. 43, AGU Monogr. Ser., American Geophysical Union, 1991.

Lummerzheim, D., M. Brittnacher, D. Evans, G. A. Germany, G. K. Parks, M. H. Rees, and J. F. Spann, High time resolution study of the hemispheric power carried by energetic electrons into the ionosphere during the May 19/20, 1996 auroral activity, *Geophys. Res. Lett.*, *24*, 987, 1997.

McPherron, R. L., Physical processes producing magnetospheric substorms and magnetic storms, in *Geomagnetism*, edited by J. Jacobs, vol. 4, p. 593, Academic Press, 1991.

Raeder, J., Global Magnetohydrodynamics – A Tutorial, in *Space Plasma Simulation*, edited by J. Büchner, C. T. Dum, and M. Scholer, Springer Verlag, Berlin Heidelberg New York, 2003.

Raeder, J., and N. Maynard, Foreword, *J. Geophys. Res.*, *106*, 345, 2001.

Raeder, J., Y. L. Wang, and T. Fuller-Rowell, Geomagnetic storm simulation with a coupled magnetosphere - ionosphere - thermosphere model, in *Space Weather, AGU Geophys. Monogr. Ser.*, edited by P. Song, G. Siscoe, and H. J. Singer, vol. 125, p. 377, American Geophysical Union, 2001a.

Raeder, J., et al., Global simulation of the geospace environment modeling substorm challenge event, *J. Geophys. Res.*, *106*, 381, 2001b.

Russell, C. T., Y. L. Wang, and J. Raeder, The interplanetary shock of september 24, 1998: Arrival at Earth, *J. Geophys. Res.*, *105*, 25,143, 2001.

Sibeck, D. G., and V. Angelopoulos, THEMIS science objectives and mission phases, *Space Sci. Rev.*, *this issue*, submitted, 2008.

Slinker, S. P., J. A. Fedder, and J. G. Lyon, Plasmoid formation and evolution in a numerical simulation of a substorm, *Geophys. Res. Lett.*, *22*, 859, 1995.

Sonnerup, B. U. O., and L. J. Cahill, Magnetopause structure and attitude from Explorer 12 observations, *J. Geophys. Res.*, *72*, 171, 1967.

Sonnerup, B. U. O., and L. J. Cahill, Explorer 12 observations of the magnetopause current layer, *J. Geophys. Res.*, *73*, 1757, 1968.

Strangeway, R. J., and J. Raeder, On the transition from collisionless to collisional magnetohydrodynamics, *J. Geophys. Res.*, *106*, 1955, 2001.

Toth, G., The $\nabla \cdot B$ constraint in shock-capturing magnetohydrodynamics codes, *J. Comp. Phys.*, *161*, 605, 2000.

Tufte, E. R., *Envisioning information*, Graphics Press, Cheshire, 1990.

Vasyliunas, V. M., Mathematical models of magnetospheric convection and its coupling to the ionosphere, in *Particles and Fields in the Magnetosphere*, p. 61, Dordrecht, Netherlands: D. Reidel, 1970.

Wiltberger, M., T. I. Pulkkinen, J. G. Lyon, and C. C. Goodrich, MHD simulation of the magnetotail during the December 10, 1996, substorm, *J. Geophys. Res.*, *105*, 27,649, 2000.

Zalesak, S. T., Fully multidimensional flux-corrected transport, *J. Comp. Phys.*, *31*, 355, 1979.

Zalesak, S. T., Very high order pseudospectral flux-corrected transport (FCT) algorithms for conservation laws, in *Proceedings of the Fourth IMACS International Symposium on Computer Methods for Partial Differential Equations*, edited by R. Vichnevetsky and R. S. Stepleman, p. 126, IMACS, Rutgers University, New Brunswick, 1981.